

Changes in Monkey Crystalline Lens Spherical Aberration During Simulated Accommodation in a Lens Stretcher

Bianca Maceo Heilman,^{1,2} Fabrice Manns,^{1,2} Alberto de Castro,³ Heather Durkee,^{1,2} Esdras Arrieta,¹ Susana Marcos,³ and Jean-Marie Parel^{1,2,4}

¹Ophthalmic Biophysics Center, Bascom Palmer Eye Institute, Miami, Florida, United States

²Biomedical Optics and Laser Laboratory, Department of Biomedical Engineering, University of Miami College of Engineering, Coral Gables, Florida, United States

³Instituto de Óptica, Consejo Superior de Investigaciones Científicas, Madrid, Spain

⁴Vision Cooperative Research Centre, Brien Holden Vision Institute, University of New South Wales, Sydney, New South Wales, Australia

Correspondence: Fabrice Manns, Bascom Palmer Eye Institute, 1638 NW 10 Avenue, Miami, FL 33136, USA; fmanns@miami.edu.

Submitted: November 11, 2014

Accepted: February 4, 2015

Citation: Maceo Heilman B, Manns F, de Castro A, et al. Changes in monkey crystalline lens spherical aberration during simulated accommodation in a lens stretcher. *Invest Ophthalmol Vis Sci*. 2015;56:1743-1750. DOI:10.1167/iovs.14-16057

PURPOSE. The purpose of this study was to quantify accommodation-induced changes in the spherical aberration of cynomolgus monkey lenses.

METHODS. Twenty-four lenses from 20 cynomolgus monkeys (*Macaca fascicularis*; 4.4–16.0 years of age; postmortem time 13.5 ± 13.0 hours) were mounted in a lens stretcher. Lens spherical aberration was measured in the unstretched (accommodated) and stretched (relaxed) states with a laser ray tracing system that delivered 51 equally spaced parallel rays along 1 meridian of the lens over the central 6-mm optical zone. A camera mounted below the lens was used to measure the ray height at multiple positions along the optical axis. For each entrance ray, the change in ray height with axial position was fitted with a third-order polynomial. The effective paraxial focal length and Zernike spherical aberration coefficients corresponding to a 6-mm pupil diameter were extracted from the fitted values.

RESULTS. The unstretched lens power decreased with age from 59.3 ± 4.0 diopters (D) for young lenses to 45.7 ± 3.1 D for older lenses. The unstretched lens shifted toward less negative spherical aberration with age, from -6.3 ± 0.7 μm for young lenses to -5.0 ± 0.5 μm for older lenses. The power and spherical aberration of lenses in the stretched state were independent of age, with values of 33.5 ± 3.4 D and -2.6 ± 0.5 μm , respectively.

CONCLUSIONS. Spherical aberration is negative in cynomolgus monkey lenses and becomes more negative with accommodation. These results are in good agreement with the predicted values using computational ray tracing in a lens model with a reconstructed gradient refractive index. The spherical aberration of the unstretched lens becomes less negative with age.

Keywords: crystalline lens, laser ray tracing, optics, spherical aberration

The ability of the human eye to accommodate is due to a change in the shape of the crystalline lens, which produces a change in lens optical power. The change in lens shape with accommodation also produces a change in the aberrations of the lens and the whole eye.^{1–4} The changes in lens and ocular aberrations with accommodation are of special interest because they impact retinal image quality and are therefore factors in determining the best focus position of the eye. Changes in ocular spherical aberration with accommodation could also play a role in the development of refractive error and in determining the optical accommodative response.^{5–9}

Overall, studies in human and non-human primates (NHPs) have shown that the spherical aberration of the eye shifts toward more negative values with accommodation.^{1–4,10–15} It is difficult to obtain direct in vivo spherical aberration measurements of the lens due to its position behind the cornea and iris. The aberrations of the lens can be estimated by measuring whole-eye aberrations and subtracting the aberrations of the anterior and posterior corneal surfaces.^{16,17} In a study by Smith et al.,¹⁸ the spherical aberration of in vivo human lenses was

predicted by measuring the aberrations of the whole eye and subtracting those of the anterior corneal surface, based on the measured anterior corneal radius of curvature and asphericity, and the predicted posterior corneal surface, based on the estimated posterior corneal radius of curvature and asphericity. The mean spherical aberration of the lens was found to be negative over a wide range of possible posterior corneal surface values. With the availability of commercial devices that measure the posterior corneal surface, it is now possible to calculate in vivo lens spherical aberrations more accurately, using ocular biometry and aberrometry combined with optical modeling.

The development of lens stretching devices that reproduce accommodation in postmortem tissue has allowed for the study of lens accommodation in vitro.^{12,13,19–22} With these devices, it is possible to directly measure the spherical aberration of the lens and its changes with simulated accommodation. The techniques used thus far to measure lens spherical aberration have their respective limitations. Glasser and Campbell¹² measured the longitudinal spherical aberration of 27 human lenses in a lens stretcher by using a laser ray tracing (LRT)

system. The lenses were placed in a tank filled with saline and an HeNe laser delivered multiple beams along the lens. Drops of paint were added to scatter the light, and a side-facing camera was used to capture images of the beams projected along the lens. Their results showed that lens spherical aberration becomes more negative with accommodation and more positive with age. This study demonstrated the principle of LRT to measure lens spherical aberration and provided insight into the general behavior of the lens. However, this photographic LRT technique is subject to measurement uncertainty because it is difficult to quantify the path of the rays in the paraxial region. This makes it challenging to determine the paraxial focal length of the lens and therefore to quantify the spherical aberration with high precision. In a more recent study by Roorda and Glasser,¹³ the technique was refined to produce a three-dimensional wavefront measurement of the lens by using two cameras and measurements of the wavefront slopes rather than the intersections of the rays along the optical axis. However, lens spherical aberration data were reported only for one macaque monkey lens.

Simulations based on a reconstructed gradient refractive index (GRIN) have been used to predict spherical aberration in ex vivo lenses and its changes with accommodation.²³ In that study, the lens shape and GRIN were reconstructed from optical coherence tomography (OCT) images.^{24,25} A numerical ray trace was performed through the reconstructed lens to predict the spherical aberration. The study found that the lens spherical aberration becomes more negative with accommodation, similar to previous findings.

In the present study, we used a direct technique to measure the changes in lens spherical aberration with accommodation in cynomolgus monkey lenses, using measurements based on LRT. We combined OCT with LRT to allow for direct measurement of lens spherical aberration during simulated accommodation in a lens stretcher. The measurements produced in this study are in good agreement with the results obtained from numerical ray tracing based on a model of the reconstructed lens,²³ which serves to validate the GRIN reconstruction technique.

METHODS

Donor Tissue

Data were acquired using 24 lenses from 20 cynomolgus monkeys (*Macaca fascicularis*; ages 4.4–16.0 years; postmortem time 13.5 ± 13.0 hours). In the four cases where the left and right eyes were measured in the same monkeys, there was a high degree of similarity between eyes. Power and spherical aberration data were averaged for the analysis in the case where both eyes were measured. All experiments adhered to the Association for Research in Vision and Ophthalmology Statement for the Use of Animals in Ophthalmic and Visual Research. The eyes were obtained from the Division of Veterinary Resources at the University of Miami as part of a tissue-sharing protocol and were used in accordance with Institutional Animal Care and Use Guidelines. The eyes were enucleated immediately after monkeys were euthanized and wrapped in gauze and stored in a closed container. No animals were euthanized for the sole purpose of this study. Upon arrival at the laboratory, all eyes were either prepared for stretching experiments or refrigerated at 4°C.²⁶

Stretching Experiments

A custom-built second-generation lens stretching system, Ex-Vivo Accommodation Simulator II (EVAS II), was used to

reproduce dis-accommodation in postmortem lenses. The lens stretcher and the tissue preparation protocol have been published previously.^{19,20} In summary, the whole globe was bonded to eight scleral shoes to preserve the globe's shape during the dissection and stretching experiments. Once the shoes were bonded to the sclera, the posterior pole was sectioned, and the cornea and iris were removed. Incisions were made between the sclera of adjacent shoes to create eight independent segments for stretching. Following the dissection, the tissue preparation, consisting of the ciliary body, zonular fibers, crystalline lens, and segmented sclera, was mounted into the lens stretcher. In the present study, the effective power and spherical aberration of lenses in the unstretched and fully stretched states (shoes displaced radially by 2.5 mm) were measured with a laser ray tracing system.

Laser Ray Tracing System

The LRT system was developed using the delivery optics from a custom-built time-domain (TD)-OCT system coupled with the EVAS II lens stretcher (Fig. 1, left).^{22,27} The OCT system uses a superluminescent diode with a central wavelength of 825 nm and a bandwidth of 25 nm.²⁷ The beam delivery system is mounted on a 3-axis translation stage to allow precise centering of the beam in the transverse direction. The beam was aligned on the crystalline lens apex prior to stretching experiments by visualizing the central OCT A-line signal intensity in real-time and adjusting the position of the delivery optics until the signal peaks corresponding to the anterior and posterior lens surfaces were maximized.

Once the beam was centered on the lens, the LRT system performed a ray trace by sequentially delivering 51 equally spaced parallel rays along one meridian of the lens over the central 6-mm optical zone. A camera module (model GP-CX261V; Panasonic, Osaka, Japan) mounted on a vertical positioning stage below the tissue chamber was used to record the spots corresponding to each individual ray (51 in total). Images were acquired at multiple axial positions along the optical axis, covering a range of up to 25 mm below the chamber (Fig. 1, right). Laser ray tracing experiments were conducted using lenses in unstretched (accommodated) and stretched (relaxed) states.

Calculation of Effective Lens Power and Spherical Aberration

A program written in MATLAB software (Mathworks, Natick, MA, USA) was used to calculate the centroid of each spot for all images. The centroid position was used as an estimate for the ray height incident on the camera, y . Figure 2 shows the measured ray heights plotted as a function of entrance ray height for a typical cynomolgus monkey lens. These graphs were generated for each axial position, z , of the camera and fitted with a third-order polynomial,

$$y(z) = y_0 + B(z) \times (b - b_0) + D(z) \times (b - b_0)^3, \quad (1)$$

where y_0 is a constant term (mm), $B(z)$ is a measure of paraxial ray path, $D(z)$ is a measure of the lens third-order spherical aberration (mm^{-2}), b is the entrance ray height (mm), and b_0 is an offset value that counts for lens decentration relative to the input ray trace (mm). Because the rays travel in a straight line, $B(z)$ and $D(z)$ are linear functions in terms of the axial position z . The slope and intercept of $B(z)$ and $D(z)$ are determined by performing a linear fit versus z (Fig. 3). The effective lens power, P_L (diopter [D]), was calculated from the slope, m_B , of the linear fit of $B(z)$ versus z (Appendix 1):

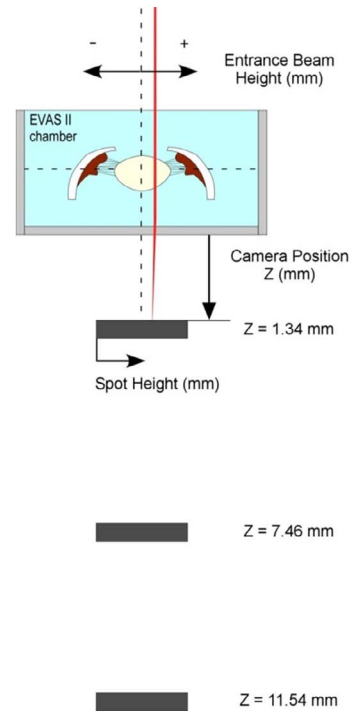
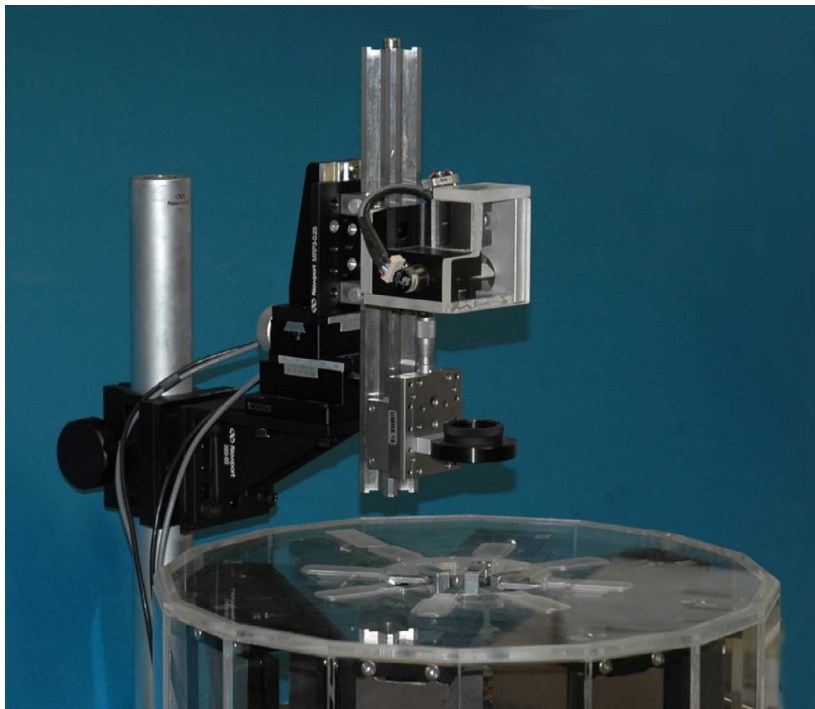


FIGURE 1. *Left:* Time-domain OCT (TD-OCT) and EVAS II system. The laser ray tracing system uses TD-OCT beam delivery optics. The beam position is centered on the crystalline lens in EVAS II. *Right:* Schematic of the beam delivery onto a crystalline lens mounted in the EVAS II tissue chamber. The position of the camera is measured as the distance z (mm) below the tissue chamber.

$$P_L = -m_B. \tag{2}$$

The Zernike spherical aberration coefficient was determined from the value of the function $D(z)$ at the paraxial focus of the lens (where $z = z_{focus}$). The Zernike spherical aberration coefficient Z_4^0 (μm) was calculated by using the Optical Society of America standard for a 6-mm optical zone based on published formulas,²⁸

$$Z_4^0 = -\frac{a^4}{24 \cdot \sqrt{5}} \cdot P_L \cdot D(z_{focus}), \tag{3}$$

where a is the pupil radius (3 mm), P_L is the effective lens power, and $D(z_{focus})$ is the value of the function at the focal point of the lens. Equation 3 is derived in Appendix 2.

RESULTS

Effective Lens Power

The effective lens power was greater in the unstretched (accommodated) state than in the stretched (unaccommodated) state, as expected. Figure 4 shows the effective lens power for cynomolgus monkey lenses plotted with respect to age. There was a significant decrease in the unstretched lens power with age ($P < 0.0001$), whereas the stretched lens power was relatively constant.

On average, the effective lens power was 59.10 ± 4.27 D for young cynomolgus monkeys (< 9.3 years old) and 46.30 ± 2.86 D for older cynomolgus monkeys (> 13.3 years old) in the

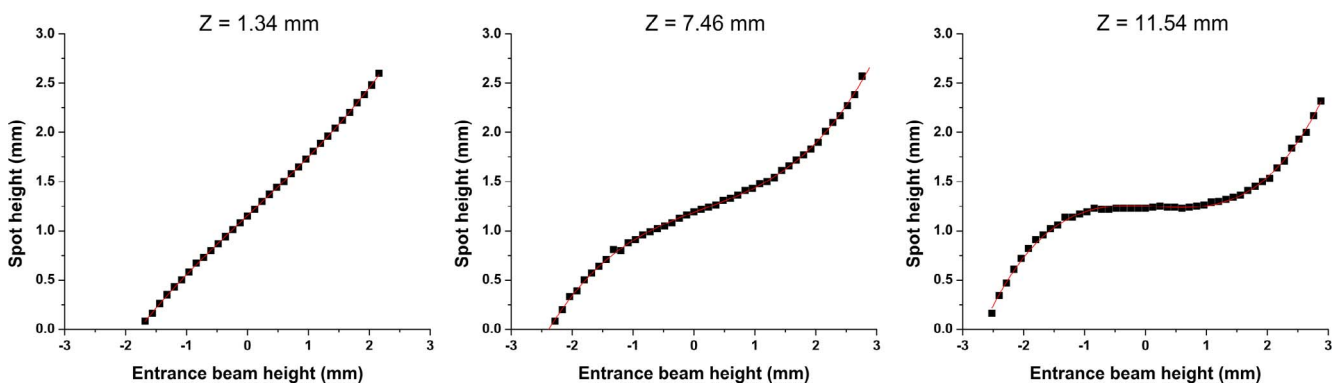


FIGURE 2. Spot height on the camera (mm) is shown as a function of entrance ray height (mm) for a typical cynomolgus monkey (age = 5.25 years; postmortem time = 2 hours) unstretched lens at $z = 1.34$ mm (*left*), $z = 7.46$ mm (*center*), and $z = 11.54$ mm (*right*). The position $z = 11.54$ mm is near the paraxial focus of the crystalline lens exhibiting the third-order behavior characteristic of spherical aberration. A third-order polynomial fitting was performed on each plot (*red*).

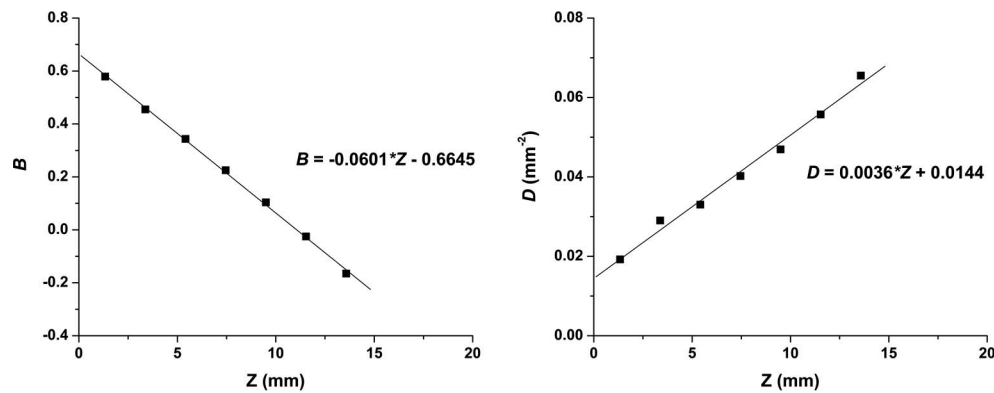


FIGURE 3. Coefficients B (left) and D (right) were plotted as a function of distance z for a typical cynomolgus monkey lens in the unstretched position. For this example, $m_B = -0.0601 \text{ mm}^{-1}$; and $m_D = 0.0036 \text{ mm}^{-3}$.

unstretched state. The average effective power was $33.55 \pm 3.41 \text{ D}$ for lenses in the stretched state.

Spherical Aberration

Figure 5 shows the Zernike spherical aberration coefficients for cynomolgus monkey lenses plotted with respect to age. Spherical aberration was more negative in the unstretched state than in the stretched state for all lenses. There was a significant positive correlation between the unstretched lens spherical aberration and age ($P = 0.002$).

On average, spherical aberration for the unstretched lens was $-6.32 \pm 0.60 \mu\text{m}$ for young cynomolgus monkeys and $-4.89 \pm 0.48 \mu\text{m}$ for older cynomolgus monkeys. The average spherical aberration was $-2.57 \pm 0.52 \mu\text{m}$ for lenses in the stretched state. Stretching experiments produced changes corresponding to the lens spherical aberration, becoming more negative with accommodation.

DISCUSSION

In this study, we demonstrated a new method to directly measure changes in the spherical aberration of the lens during simulation of accommodation using an LRT system with a translating imaging sensor. We were able to recreate the individual ray slopes, calculate the focal length, and determine the spherical aberration of the lens at the paraxial focus by recording spot images at multiple positions along the optical axis.

There was evidence that the lens is not rotationally symmetrical and that spherical aberration varies along different meridians.²⁹ In addition, it is possible that the lens stretcher could induce unexpected high-order aberrations. The current system was limited to measurements of spherical aberration along a single meridian and did not allow us to reconstruct complete two-dimensional aberration maps and quantify these effects.

Our results showed that the spherical aberration of the cynomolgus monkey lens was negative in the stretched (relaxed) state and became more negative with accommodation. We also found that the lens spherical aberration tended to become less negative with age. Based on the equivalent human age-to-primate age conversion (monkey age = human age/3) from Bito et al.,³⁰ humans become presbyopic at approximately 40 to 50 years of age, so the equivalent monkey presbyopic age is 13 to 17 years old. A linear regression was performed with the lens spherical aberration versus age to determine if there was a statistically significant age dependence. However, more data are required over a broader age range and with a more uniform distribution in order to verify if the age dependency is linear or if it follows a more complex nonlinear behavior.

Overall, these findings are consistent with those from previous in vitro studies of human lenses¹² and from the preliminary results obtained with a macaque monkey lens by Roorda and Glasser.¹³ Our results cannot be directly compared with those of Glasser and Campbell¹² because in their study the lens spherical aberration was presented as the longitudinal spherical aberration calculated for a normalized lens diameter

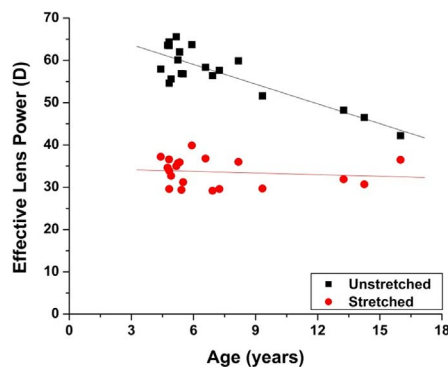


FIGURE 4. Effective lens power for cynomolgus monkey lenses with respect to age. There is a significant decrease in the unstretched lens power with age.

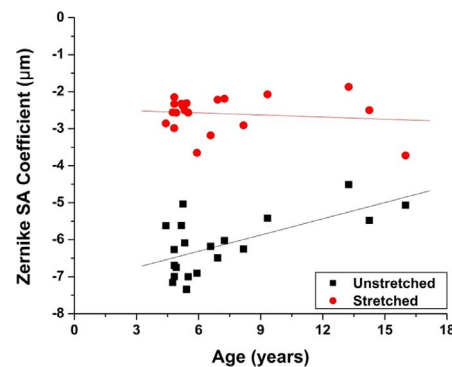


FIGURE 5. Zernike spherical aberration coefficient for cynomolgus monkey lenses plotted with respect to age. The unstretched lens shifts toward less negative spherical aberration with age.

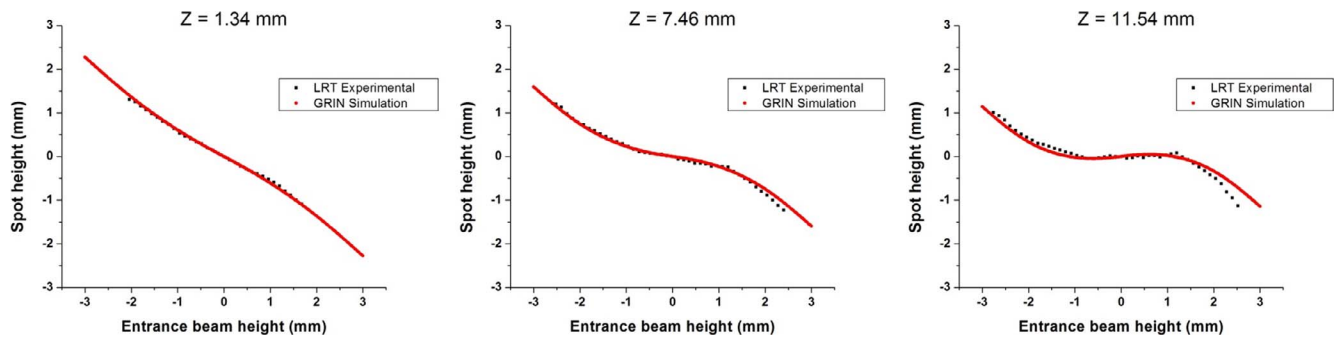


FIGURE 6. Spot diagrams for a typical cynomolgus monkey unstretched lens (age = 4.42 years; postmortem time = 26 hours). Spot heights, obtained with the laser ray tracing system, are shown in *black*, and the spot heights from the de Castro simulation²³ are shown in *red*. Laser ray trace experimental data were offset to be centered about zero to allow for direct comparison with the GRIN simulated data. The spot diagrams are shown for the $z = 1.34$ mm (*left*), $z = 7.46$ mm (*center*), and $z = 11.54$ mm (*right*) positions.

in diopters. However, the general behavior of the cynomolgus monkey lenses in our study is similar to that of human lenses.

Interestingly, the spherical aberration values measured in this study are comparable to predicted spherical aberrations obtained from the same cynomolgus monkey lenses, using the GRIN reconstruction model, by de Castro et al.²³ Seven of the cynomolgus monkey lenses used in the present study were also used in the GRIN reconstruction study by de Castro et al.²³ In that study, the lens shape and GRIN were reconstructed from OCT images. A numerical ray trace was performed through the reconstructed lens for a 6-mm pupil diameter (101 rays, ray spacing of 30 μm) to estimate the spot diagrams at the same z positions as the LRT experiment. The spot diagrams for the reconstructed GRIN lens were simulated based on the ray trace for lenses at the corresponding camera positions, z , in the unstretched and stretched states. The simulated spot diagrams are in close agreement with the measurements acquired with the LRT in the present study (Fig. 6). Moreover, the predicted lens spherical aberration based on the reconstructed GRIN lens model²³ is in good agreement with the measured spherical aberration using LRT for the seven lenses. Figure 7 shows the predicted spherical aberration versus the measured spherical aberration (Fig. 7, left), and the Bland-Altman analysis for the two different methods (Fig. 7, right). Difference between the two methods fell within ± 2 SD for all lenses, and the mean difference was -0.51 μm . The close agreement between experimental data and model predictions using these two independent methods serves to validate the method for

reconstructing the lens GRIN from OCT images of crystalline lenses.

Our study showed that the OCT beam used to image the crystalline lens in the EVAS II stretching system can also be used for the LRT system, without requiring additional optics to refocus the beam on the imaging sensor. We were able to recreate the individual ray slopes by recording spot images at multiple positions along the optical axis with an imaging sensor mounted on a translation stage below the lens. This technique solved some of the limitations of the lateral LRT technique and can also be extended to produce an aberration map by using a two-dimensional scan, similar to the method of Roorda and Glasser.¹³

One of the issues encountered by using the OCT beam as the LRT beam is that the beam is focused on the crystalline lens to provide the best quality OCT image. As a result, the beam diverges after it exits the crystalline lens. When the camera position is moved away from the lens and near the lens focus, the OCT beam becomes defocused, which reduces the quality of the spot images and the precision of the centroid calculation. To minimize this effect, spot images were recorded away from the focus near the tissue chamber, and the focus position was calculated from the linear fit of the function $B(z)$ in Equation 1. Another potential source of error in the LRT system is that the posterior window of the tissue chamber may contribute to the measured spherical aberration. To quantify the potential error introduced by the window, a ray trace analysis was performed using ray tracing software (OSLO; Lambda Research Corp, Littleton, MA, USA). Analysis showed

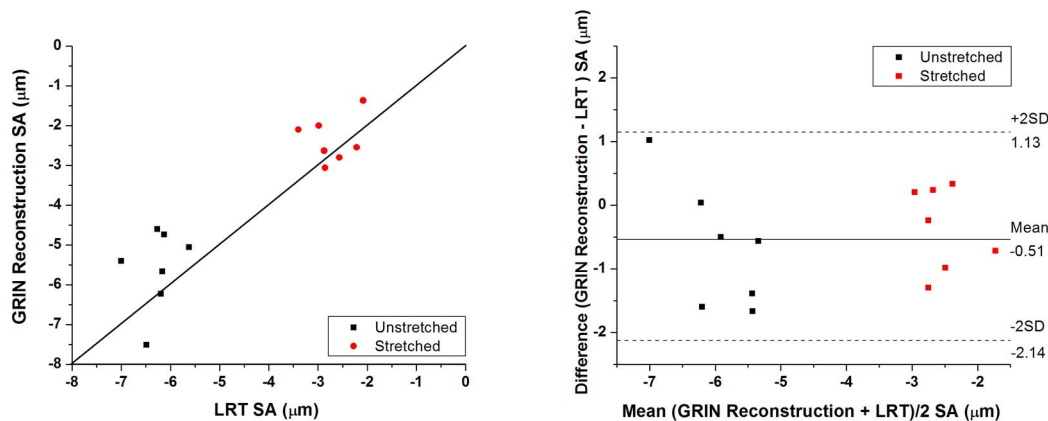


FIGURE 7. *Left*: Predicted Zernike spherical aberration based on the reconstructed GRIN lens model²² plotted with respect to the measured Zernike spherical aberration, using LRT for the same seven cynomolgus monkey lenses. *Right*: Bland-Altman plot of predicted spherical aberration versus measured spherical aberration.

that the window contributes approximately 2% error to the spherical aberration coefficient ($-0.4325 \mu\text{m}$ with the window compared to $-0.4234 \mu\text{m}$ without) compared to the crystalline lens spherical aberration, which averaged $-6.08 \pm 0.79 \mu\text{m}$ in the unstretched position and $-2.57 \pm 0.52 \mu\text{m}$ in the stretched position. The window contribution was therefore not taken into account.

In summary, we present a refined LRT method that allows for direct measurement of lens effective power and spherical aberration. Our study produced results which are in very good agreement with the results obtained from numerical ray tracing based on a model of the lens, which validates the GRIN reconstruction technique. Our data showed that spherical aberration is negative in cynomolgus monkey lenses and that spherical aberration becomes more negative with accommodation and becomes less negative with age. We are currently improving the instrumentation and method to enable us to measure complete higher order aberration maps of the crystalline lens during stretching.

Acknowledgments

The authors thank Shawn Kelly, Yue Yao, and Judith Birkenfeld, PhD, for assistance with data processing, and Stephen Uhlhorn for development of laboratory software and equipment. The authors also thank James Geary, Waldo Diaz, Norma Kenyon, PhD, Dora Berman-Weinberg, PhD, Diabetes Research Institute, and Julia Zaias, PhD, Division of Veterinary Research, University of Miami, for scientific support.

Supported by National Institutes of Health Grants R01EY14225, R01EY021834, and F31EY021444 Ruth L. Kirschstein National Research Service Award individual predoctoral fellowship [BM]), and center Grant P30EY14801; Australian government Cooperative Research Centre Scheme (Vision CRC); Florida Lions Eye Bank; Karl R. Olsen and Martha E. Hildebrandt; an unrestricted grant from Research to Prevent Blindness; Henri and Flore Lesieur Foundation (JMP); Spanish government Grant FIS2011-25637; and European Research Council Grants ERC-2011-AdG-294099 and CSIC iLINK+0609.

Disclosure: **B. Maceo Heilman**, None; **F. Manns**, None; **A. de Castro**, None; **H. Durkee**, None; **E. Arrieta**, None; **S. Marcos**, None; **J.-M. Parel**, None

APPENDIX 1

The measured spot heights were plotted as a function of entrance ray height (Fig. 2), and a plot was generated for each axial position, z , of the camera. Each plot was fitted with a third-order polynomial:

$$y(z) = y_0 + B(z) \times (b - b_0) + D(z) \times (b - b_0)^3. \quad (1)$$

Because the ray is a straight line, $B(z)$ and $D(z)$ are linear functions

$$B(z) = B_0 + m_B \cdot z \quad (A1)$$

$$D(z) = D_0 + m_D \cdot z, \quad (A2)$$

where B_0 and D_0 (mm^{-2}) are constant terms, m_B (mm^{-1}) and m_D (mm^{-3}) are the slopes of the linear fits, and z is the position of the camera (mm). To simplify the description, we assumed $b_0 = 0$, because b_0 is a term included to take into account lateral offset in the experiment.

In paraxial approximation, the spherical aberration of the lens is zero, $D(z) = 0$, which gives

$$y(z) = y_0 + (B_0 + m_B \cdot z) \cdot b. \quad (A3)$$

In our experimental setup, with the notation of Figure A1, the output ray height and slope are related to the input ray height and slopes by the following formula, expressed in paraxial matrix notation,

$$\begin{bmatrix} y \\ \theta' \end{bmatrix} = \begin{bmatrix} 1 - d_p \cdot \frac{P_L}{n_a} - P_L \left(\frac{d_w}{n_w} + z \right) & d_p + d_w \frac{n_a}{n_w} + n_a \cdot z \\ -P_L & n_a \end{bmatrix} \cdot \begin{bmatrix} b \\ \theta \end{bmatrix}, \quad (A4)$$

where y is the measured ray height on the camera (mm), $\theta' = dy/dz$ is the output ray slope, d_p is the distance between the posterior surface of the lens and the anterior surface of the tissue chamber window (mm), P_L is the measured effective power of the lens (D), n_a is the refractive index of the medium ($n_a = 1.336$), d_w is the thickness of the glass window (mm), n_w is the refractive index of the window ($n_w = 1.510$), b is the entrance ray height (mm), and θ is the incident angle ($^\circ$). In our experiments, the incident angle is equal to zero ($\theta = 0$). In this case, Equation A7 can be simplified to

$$y(z) = \left[1 - \frac{P_L \cdot d_p}{n_a} - P_L \left(\frac{d_w}{n_w} + z \right) \right] \cdot b \quad (A5a)$$

$$\theta' = \frac{dy}{dz} = -P_L \cdot b. \quad (A5b)$$

Equation A5b shows that the effective lens power is related to the output ray slope and entrance ray height. Comparison of Equation A5b with Equation A3 gives the following final result, Equation 2 in the Methods:

$$P_L = -m_B.$$

The position of the lens focus is found by solving for the value of z that gives $y = 0$ in Equation A5a, independent of b , which gives

$$z_{focus} = \frac{1}{P_L} - \frac{d_p}{n_a} - \frac{d_w}{n_w}. \quad (A6)$$

APPENDIX 2

In order to directly compare spherical aberration coefficients, $D(z_{focus})$, measured with the LRT system with previously published data, the values were converted to Zernike spherical aberration coefficients. Higher-order aberrations other than spherical aberration were assumed to be negligible.

For each lens, the spot diagram at the focus was fitted with a third-order term²⁸:

$$\Delta y(b) = D(z_{focus}) \cdot b^3, \quad (A7)$$

where Δy is the ray aberration equivalent to the spot shift on the camera (mm) at the paraxial focus of the lens, b is the entrance ray height (mm), and $D(z_{focus})$ is the value of the function D at the lens focus (mm^{-2}). The contribution of spherical aberration to the Zernike wavefront aberration^{31,32} is

$$W(b) = 6\sqrt{5} \cdot Z_4^0 \cdot \left(\frac{b}{a} \right)^4, \quad (A8)$$

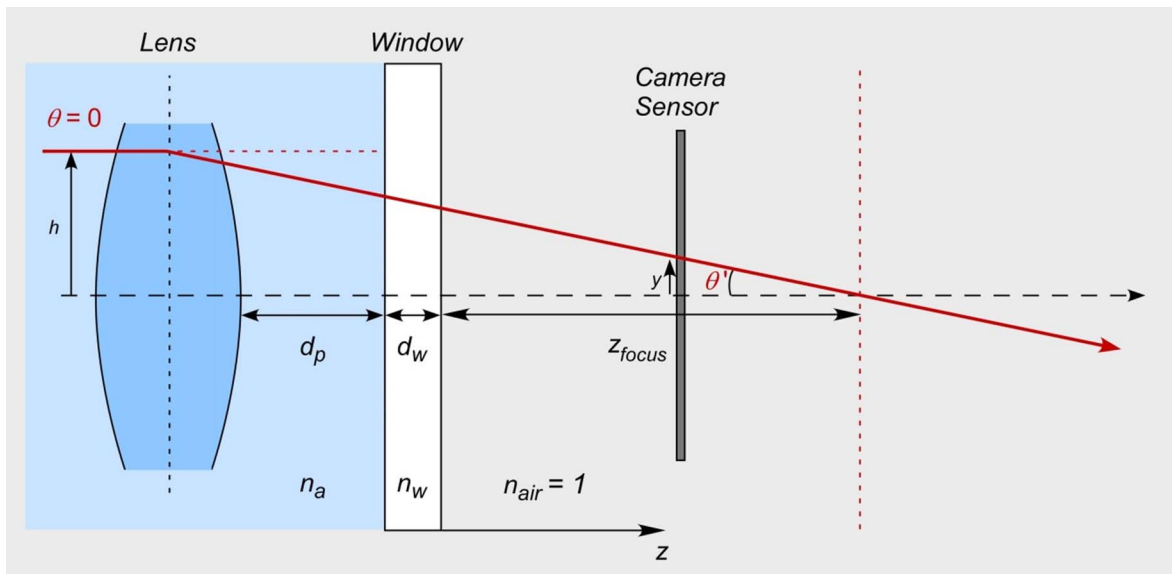


FIGURE A1. Schematic of LRT beam propagating through the lens along direction z . Term b is the entrance ray height, θ is the incident angle ($\theta = 0$), d_p is the distance between the posterior surface of the lens and the window of the tissue chamber, n_a is the refractive index of the medium, d_w is the thickness of the window, n_w is the refractive index of the window, n_{air} is the refractive index of air ($n_{air} = 1$), y is the ray height incident on the camera, $\theta' = dy/dz$ is the output ray slope, and z_{focus} is the distance between the posterior window surface and the lens focus along the optical axis.

where W is the wavefront aberration (μm), Z_4^0 is the Zernike spherical aberration coefficient (μm), b is the input ray height (mm), and a is the pupil radius (mm).

Using Optical Society of America recommended standards for reporting optical aberrations, the relationship between ray aberration and wave aberration^{31,32} is

$$\Delta y(b) = -\frac{R}{n'} \cdot \frac{dW}{db}, \quad (\text{A9})$$

where R is the radius of the reference wavefront and n' is the refractive index of the image space. In our case, for rays entering the lens parallel to the axis, R is the effective focal length, f' , of the lens.

In terms of the effective lens power, P_L ,

$$\Delta y(b) = -\frac{1}{P_L} \cdot \frac{dW}{db}, \quad (\text{A10})$$

where $P_L = n'/f'$. Taking the derivative of Equation A8,

$$\frac{dW}{db} = \frac{24\sqrt{5}}{a^4} \cdot Z_4^0 \cdot b^3. \quad (\text{A11})$$

Combining Equations A10 and A11 results in

$$\Delta y(b) = -\frac{24\sqrt{5}}{P_L \cdot a^4} \cdot Z_4^0 \cdot b^3. \quad (\text{A12})$$

Combining Equations A7 and A12 results in

$$D = -\frac{24\sqrt{5}}{a^4} \cdot \frac{Z_4^0}{P_L}. \quad (\text{A13})$$

Solving for Z_4^0 gives:

$$Z_4^0 = -\frac{a^4}{24\sqrt{5}} \cdot P_L \cdot D. \quad (\text{A14})$$

References

- Ivanoff A. About the spherical aberration of the eye. *J Opt Soc Am.* 1956;46:901-903.
- Jenkins TC. Aberrations of the eye and their effects on vision. Part 1. *Br J Physiol Opt.* 1963;20:59-91.
- He JC, Burns SA, Marcos S. Monochromatic aberrations in the accommodated human eye. *Vision Res.* 2000;40:41-48.
- Vilupuru AS, Roorda A, Glasser A. Spatially variant changes in lens power during ocular accommodation in a rhesus monkey eye. *J Vis.* 2004;4(4):299-309.
- Charman WN, Tucker J. Dependence of accommodation response on the spatial frequency spectrum of the observed object. *Vision Res.* 1977;17:129-139.
- Walsh G, Charman WN. The effect of defocus on the contrast and phase of the retinal image of a sinusoidal grating. *Ophthalmic Physiol Opt.* 1989;9:398-404.
- Wilson BJ, Decker KE, Roorda A. Monochromatic aberrations provide an odd-error cue to focus direction. *J Opt Soc Am.* 2002;19:833-839.
- Whatman A, Zimmermann F, Martinez A, et al. Influence of accommodation on off-axis refractive errors in myopic eyes. *J Vis.* 2009;9(3):14.1-14.13.
- Thibos LN, Bradley A, Liu T, Lopez-Gil N. Spherical aberration and the sign of defocus. *Optom Vis Sci.* 2013;90:1284-1291.
- Koomen M, Tousey R, Scolnik R. The spherical aberration of the eye. *J Opt Soc Am A Opt Image Sci Vis.* 1949;39:370-376.
- Atchison DA, Collins MJ, Wildsoet CF, Christensen J, Waterworth MD. Measurement of monochromatic ocular aberrations of human eyes as a function of accommodation by the Howland aberroscope technique. *Vis Res.* 1995;35:313-333.
- Glasser A, Campbell MCW. Presbyopia and the optical changes in the human crystalline lens with age. *Vision Res.* 1998;38:209-229.
- Roorda A, Glasser A. Wave aberrations of the isolated crystalline lens. *J Vis.* 2004;4(4):250-261.

14. Gamba E, Sawides L, Dorronsoro C, Marcos S. Accommodative lag and fluctuations when optical aberrations are manipulated. *J Vis.* 2009;9(6):1-15.
15. Cheng H, Barnett JK, Vilupuru AS, et al. A population study on changes in wave aberrations with accommodation. *J Vis.* 2004;4(4):272-280.
16. El Hage SG, Berny F. Contribution of the crystalline lens to the spherical aberration of the eye. *J Opt Soc Am.* 1973;63:205-211.
17. Artal P, Berrio E, Guirao A, Piers P. Contribution of the cornea and internal surfaces to the change of ocular aberrations with age. *J Opt Soc Am.* 2002;19:137-143.
18. Smith G, Cox MJ, Calver R, Garner LE. The spherical aberration of the crystalline lens of the human eye. *Vision Res.* 2001;41:235-243.
19. Manns F, Parel JM, Denham D, et al. Optomechanical response of human and monkey lenses in a lens stretcher. *Invest Ophthalmol Vis Sci.* 2007;48:3260-3268.
20. Ehrmann K, Ho A, Parel J-M. Biomechanical analysis of the accommodative apparatus in primates. *Clin Exp Optom.* 2008;91:302-312.
21. Augusteyn RC, Mohamed A, Nankivil D, et al. Age-dependence of the optomechanical responses of ex vivo human lenses from India and the USA, and the force required to produce these in a lens stretcher: the similarity to in vivo disaccommodation. *Vision Res.* 2011;51:1667-1678.
22. Maceo BM, Manns F, Borja B, et al. Contribution of the crystalline lens gradient refractive index to the accommodation amplitude in non-human primates: in vitro studies. *J Vis.* 2011;13(11):23.
23. de Castro A, Birkenfeld J, Maceo B, et al. Influence of shape and gradient refractive index in the accommodative changes of spherical aberration in nonhuman primate crystalline lenses. *Invest Ophthalmol Vis Sci.* 2013;54:6197-6207.
24. de Castro A, Ortiz S, Gamba E, Siedlecki D, Marcos S. Three-dimensional reconstruction of the crystalline lens gradient index distribution from OCT imaging. *Opt Express.* 2010;18:21905-21917.
25. Birkenfeld J, de Castro A, Ortiz S, Pascual D, Marcos S. Contribution of the gradient refractive index and shape to the crystalline lens spherical aberration and astigmatism. *Vision Res.* 2013;86:27-34.
26. Nankivil D, Manns F, Arrieta-Quintero E, et al. Effect of anterior zonule transection on the change in lens diameter and power in cynomolgus monkeys during simulated accommodation. *Invest Ophthalmol Vis Sci.* 2009;50:4017-4021.
27. Uhlhorn, SR, Borja D, Manns F, Parel JM. Refractive index measurement of the isolated crystalline lens using optical coherence tomography. *Vision Res.* 2008;48:2732-2738.
28. Welford WT. Optical invariants. In: Pike ER, Welford WT, eds. *Aberrations of Optical Systems.* Bristol, UK: Adam Hilger Imprint, IOP Publishing Ltd.; 1986:79-129.
29. Sun M, Birkenfeld J, de Castro A, Ortiz S, Marcos SOCT. 3-D surface topography of isolated human crystalline lenses. *Biomed Opt Express.* 2014;5:3547-3561.
30. Bito LZ, DeRousseau CJ, Kaufman PL, Bito JW. Age-dependent loss of accommodative amplitude in rhesus monkeys: an animal model for presbyopia. *Invest Ophthalmol Vis Sci.* 1982;23:23-31.
31. Thibos LN, Applegate RA, Schwiegerling JT, Webb R. VSIA Standards Taskforce Members. Vision science and its applications. Standards for reporting the optical aberrations of eyes. *J Refract Surg.* 2002;18:S652-S660.
32. Thibos LN, Applegate RA, Schwiegerling JT, Webb R; VSIA Standards Taskforce Members. Appendix A: Optical Society of America's standards for reporting optical aberrations. In: Porter J, Queener H, Lin J, Thorn K, Awwal AAS, eds. *Adaptive Optics for Vision Science: Principles, Practices, Design and Applications.* Hoboken, NJ: John Wiley & Sons, Inc.: 2006; 511-528.